Exploring the Electronic Dimensionality of Ternary and Quaternary Rhodium Halides

David Liu[ε], Noah P. Holzapfel[ε], Alexander Milder, and Patrick M. Woodward*

Department of Chemistry and Biochemistry, The Ohio State University, 100 W. 18th Avenue, Columbus, Ohio 43210, United States

woodward.55@osu.edu

Abstract:

The synthesis, crystal structures, and optical properties of four ternary and six quaternary halides containing the Rh^{3+} ion are reported here. Rb_3RhCl_6 adopts a monoclinic structure with isolated $[RhCl_6]^{3-}$ octahedra. $Rb_3Rh_2Cl_9$, $Cs_3Rh_2Cl_9$, and $Cs_3Rh_2Br_9$ crystallize in a vacancy ordered variant of the 6H hexagonal perovskite structure, which contains isolated $Rh_2X_9^{3-}$ (X = Cl, Br) dimers of face-sharing octahedra. $Cs_2AgRhCl_6$ and $Cs_2NaRhCl_6$ adopt the 12R rhombohedral perovskite structure, featuring $[M_2RhCl_{12}]^{7-}$ face-sharing octahedral trimers, connected to one another through rhodium-centered octahedra. $A_4AgRhCl_8$ and $A_4AgRhBr_8$ (A = $CH_3CH_2CH_2CH_2NH_3^+$, $(CH_3)_2CHCH_2CH_2NH_3)^+$) crystallize in a cation-ordered variant of the *n* = 1 Ruddlesden Popper structure, which features layers of corner-connected octahedra with a chessboard ordering of Ag^+ and Rh^{3+} ions separated by double layers of organic cations. The diffuse reflectance spectra of all compositions studied feature peaks in the visible that can be attributed to spin-allowed *d*-to-*d* transitions and peaks in the UV that arise from charge transfer transitions. Electronic structure calculations reveal moderate Rh–X–Ag hybridization when rhodium- and silver-centered octahedra share corners, but minimal hybridization when they share faces. Many of the compositions studied have an electronic structure that is effectively zero-dimensional, but $Cs_2AgRhCl_6$ is found to possess a two-dimensional electronic structure. The results are instructive for controlling the electronic dimensionality of compositionally complex halide perovskite derivatives.

INTRODUCTION

Inorganic halide perovskites with the formula ABX_3, show great potential for various applications due to their promising optoelectronic properties. Significant research efforts have focused on Pb-based compositions, $APbX_3$ ($A = Cs^+$, $CH_3NH_3^+$; $X = Cl^-$, Br^-, I^-), since their initial demonstration as solar absorbing materials in 2009.[1–7] Extensive research in this area has resulted in perovskite solar cells with power conversion efficiencies reaching ~26%.[8] While the high efficiencies and solution processability make halide perovskites attractive for photovoltaic applications, concerns over the toxicity of lead persist. These concerns are heightened by the relative ease of degradation when exposed to moist atmospheres, and the limited thermal stability of the Pb-based materials.[9,10]

To address these concerns, some researchers have turned to double perovskites in hopes of finding non-toxic compositions with favorable optoelectronic properties.[11] In the double perovskite structure, the Pb^{2+} cations are replaced with a 1:1 mixture of M^+ and M^{3+} cations leading to the formula to $A_2M^+M^{3+}X_6$. Of the halide double perovskites, $Cs_2AgBiBr_6$, and to a lesser extent $(CH_3NH)_2AgBiBr_6$, have been the most extensively studied for photovoltaic applications, but the indirect and relatively large band gaps of these materials motivates further examination of double perovskite compositional space.[12,13] Computational studies have identified $A_2(In^+/Tl^+)(Sb^{3+}/Bi^{3+})X_6$ compositions as having both direct band gaps and strong optical absorption characteristics.[14] While these compounds have favorable electronic structures, they come with significant limitations. The toxicity of thallium, and to a lesser extent antimony, would not be an improvement over the current lead-based compositions, and the oxidative instability of In^+ is a significant challenge.

Computational studies by Varadwaj et al. of $A_2AgRhCl_6$ ($A = Li^+$, Na^+, K^+, Rb^+, Cs^+) with the cubic double perovskite structure, predict that such compositions would have small direct band gaps and large optical absorption coefficients. $Cs_2AgRhCl_6$ appears to be the most promising of these materials as it is predicted to be both dynamically and mechanically stable, but it has yet to be synthetically realized.[15] Recently, Holzapfel et al. reported a series of 2H hexagonal double perovskites $(CH_3NH_3)_2MRhX_6$ ($M = Na^+$, Ag^+; $X = Cl^-$, Br^-). Despite the presence of one-dimensional chains of face sharing octahedra, the absorption spectra mirrored the localized absorption characteristics of $[RhX_6]^{3-}$ complex ions, suggesting a zero-dimensional electronic

structure. The calculated band structures agreed with this description, revealing relatively flat bands near the Fermi energy.[16]

To explore the potential of halide double perovskites containing the diamagnetic Rh^{3+} ion, new compounds with higher dimensional band structures are sought. The calculations discussed above provide a clear motivation to prepare double perovskites such as $Cs_2AgRhCl_6$ to realize a three-dimensional electronic structure.[15] Compounds with a two-dimensional band structure might be obtained by using larger organic cations to stabilize a layered perovskite structure. Previous work by McClure et al. successfully used larger organic cations, such as butylammonium ($CH_3CH_2CH_2CH_2NH_3^+$, BA), to prepare hybrid layered double perovskites such as $(BA)_4AgSbBr_8$ and $(BA)_4CuInCl_8$.[17]

Herein, we explore the relationships between the crystal structure, electronic structure, and optical properties of halide perovskite derivatives containing the Rh^{3+} ion. A series of previously unknown ternary and quaternary halides have been prepared that adopt a variety of structure types, including cation-ordered hexagonal and layered perovskites. A combination of diffuse reflectance spectroscopy and electronic band structure calculations are used to evaluate the electronic structures of these compounds. The results allow us to characterize the electronic dimensionality of these compounds and correlate that dimensionality with the connectivity of the octahedral network. The findings are qualitatively generalizable to the broader family of transition metal halide compounds, and as such have implications for the design of new materials for solar energy conversion and lighting technologies.

EXPERIMENTAL

CsCl (Alfa Aesar, 99.9%), RbCl (Research Products International, Lot #123989-146209), NaCl (GFS Chemicals, 99%), CsBr (Alfa Aesar, 99.9%), AgBr (Alfa Aesar, 99.5%) and $RhCl_3 \cdot 3H_2O$ (Matthey Bishop, Lot #33313) were used as received. AgCl was synthesized on a gram scale via precipitation reaction between KCl (Fisher Scientific, 99.8%) and $AgNO_3$ (Alfa Aesar, 99.9%). The resulting white product was washed three times with deionized H_2O and dried overnight via vacuum filtration. While drying, the filter flask was covered with foil to prevent photoreduction of Ag(I) into Ag(0). Butylammonium chloride $CH_3CH_2CH_2CH_2NH_3Cl$ (BACl) and isopropylammonium chloride $(CH_3)_2CHCH_2CH_2NH_3Cl$ (IPACl) were synthesized by the neutralization of butylamine (Sigma-Aldrich, 99.5%) or isopentylamine (Alfa Aesar, 99%) with

HCl (Fisher Scientific, 37%) in cold (~ 0 °C) ethanol (Deacon Labs, 200 proof). After neutralization, the solutions were heated to 80 °C and evaporated to dryness. Similar methods were used to prepare the organic ammonium bromide salts using HBr (Sigma-Aldrich, 48%). The resulting white powders were ground and transferred to a glass vial, which was placed under vacuum overnight. Typical yields were > 90%. After preparation, the salts were stored in a desiccator until use.

$Cs_3Rh_2Cl_9$, $Cs_3Rh_2Br_9$, and $Rb_3Rh_2Br_9$ were prepared by adding stoichiometric amounts of $RhCl_3 \cdot 3H_2O$ and the appropriate alkali metal halide to 23 mL Teflon liners. Next, 5 mL of either hydrochloric or hydrobromic acid per gram of expected product was added and the solutions were magnetically stirred for 30 minutes. The liners were then sealed in stainless-steel autoclaves and heated to 130 °C for 12 hours, before cooling to room temperature at a rate of 1.5 °C/hr. Finally, the resulting powder products were collected via vacuum filtration and washed with diethyl ether (Fisher Scientific, 99.9%).

$Cs_2AgRhCl_6$ and Rb_3RhCl_6 were prepared via traditional solid-state methods by grinding stoichiometric amounts of CsCl/RbCl, AgCl, and $RhCl_3 \cdot 3H_2O$ together for a duration of 20 minutes. After grinding the powder was added to an alumina crucible and heated to 250 °C to dehydrate the $RhCl_3 \cdot 3H_2O$. The crucible was then heated to 350 °C in a box furnace for 48 hours. Finally, the resulting dark gray $Cs_2AgRhCl_6$ powder was washed with deionized water. $Cs_2NaRhCl_6$ was prepared in a similar manner by grinding stoichiometric amounts of CsCl, NaCl, and $RhCl_3 \cdot 3H_2O$ together for a duration of 20 minutes. The resulting mixture was added to an alumina crucible and heated to 250 °C to dehydrate the $RhCl_3 \cdot 3H_2O$. The crucible was then sealed in an evacuated quartz ampoule and heated to 450 °C for 48 hours. It was determined that at least three heating cycles with intermittent grinding steps were necessary to obtain a near phase-pure pink powder.

$Cs_2AgRhCl_6$ single crystals were prepared by adding stoichiometric amounts of $RhCl_3 \cdot 3H_2O$, AgCl, and CsCl to a Teflon liner. Following this, 40 mL of hydrochloric acid per gram of expected product was added and the solution was magnetically stirred for 30 minutes. The liner was then sealed in a stainless-steel autoclave and heated to 150 °C for 12 hours, before cooling to room temperature at a rate of 1.5 °C/hr. The resulting crystals were collected via vacuum filtration and washed with ethanol.

$(BA)_4AgRhCl_8$ and $(IPA)_4AgRhCl_8$ were prepared by adding 2 mmol of either BACl or IPACl, 0.5 mmol of AgCl, and 0.5 mmol of $RhCl_3 \cdot 3H_2O$ to a 23 mL Teflon liner. Next, 5 mL of HCl was added and the solutions were magnetically stirred for 30 minutes. The liners were then sealed in stainless-steel autoclaves and placed in a box furnace that was heated to 130 °C for 10 hours and then allowed to cool to room temperature at a rate of 3 °C per hour. The violet crystals were collected via vacuum filtration and washed with isopropyl alcohol (Fisher Scientific, histological grade). The bromide compositions, which are black in color, were prepared in a similar manner. Powder samples were obtained by grinding the as-prepared crystals with agate mortar and pestle. Single crystal XRD studies of these compositions were unsuccessful for a variety of reasons. The single crystals grew as thin flexible sheets with multiple crystals grown on top of one another. This presented challenges in isolating a single grain necessary for single crystal diffraction studies. Even when a crystal was isolated, the wafer-thin morphology made it difficult to mount the crystal so that it did not move during data collection. Even when these challenges were overcome, the data quality was not suitable for structure solution and refinement.

Laboratory powder X-ray diffraction (PXRD) data were collected on a Bruker D8 Advance powder diffractometer (40 kV, 40 mA, sealed Cu X-ray tube) equipped with a Lynxeye XE-T position-sensitive detector. The data were collected with an incident beam monochromator (Johansson type SiO_2 crystal) that selects only Cu $K\alpha_1$ radiation (λ = 1.5406 Å). Synchrotron powder X-ray diffraction was collected at 295 K for the half angular range on the 11-BM beamline at Argonne National Lab. Samples were diluted by grinding the prepared powders with amorphous SiO_2 (GFS Chemicals, for chromatography) to mitigate sample absorption. Samples were packed into 0.8 mm Kapton capillaries and sealed with clay. Rietveld refinements of the synchrotron PXRD data were carried out using the TOPAS-Academic (Version 6) software package to determine the crystal structure.[18] Crystal structure images were generated in Vesta 3.[19]

UV-visible diffuse reflectance spectra (DRS) were collected from 250 nm to 800 nm with a PerkinElmer Lambda 950 spectrometer equipped with a 60 mm InGaAs integration sphere. The spectrometer was calibrated using a Labsphere Certified Reflectance Standard. For measurements, approximately 15 mg of sample was diluted in 200 mg of $BaSO_4$ (Sigma-Aldrich, 99.99%).

To confirm the expected diamagnetism, field dependent magnetization measurements were collected on a sample of $Cs_2AgRhCl_6$ from –70 to +70 kOe using a Quantum Design SQUID

MPMS-3 magnetometer. Samples were prepared by filling a gel capsule with ~100 mg of sample. The capsule was then mounted in a plastic straw.

Density functional theory (DFT) was used to calculate the electronic band structure and density of states (DOS) as implemented with the Quantum ESPRESSO (version 6.1) freeware in combination with the BURAI (version 1.3.1) GUI.[20–22] These calculations were performed using projector augmented wave potentials based on the PBE exchange-correlation functional.[23] Cutoff energies of 407.983 Rydberg and 360.808 Rydberg and a 3 × 3 × 3 k-point grid were used for the Ag- and Na-containing compounds, respectively.[24]

RESULTS

Crystal Structures

Laboratory and synchrotron PXRD data were used to verify phase purity. Compositions containing silver were found to have minor AgCl or AgBr impurity phases, < 5% by mass for $Cs_2AgRhCl_6$ and approximately 1% by mass for $(BA/IPA)_4AgRhX_8$ (X = Cl, Br). Rietveld refinements were performed to determine the crystal structures of the compounds studied. The analysis was based on synchrotron PXRD data for $Cs_3Rh_2X_9$, $Cs_2AgRhCl_6$, $(BA)_4AgRhX_8$, $(IPA)_4AgRhX_8$, and laboratory PXRD data for Rb_3RhCl_6, $Rb_3Rh_2Br_9$, $Cs_2NaRhCl_6$. A summary of the refinement methodology and detailed crystallographic information can be found in the supplemental information (Tables S1, S2), along with Rietveld fits to the PXRD patterns (Figures S1, S2). Bond valence sums (BVS) for the inorganic ions were calculated and are found to be in reasonably good agreement with the expected values, suggesting stable coordination environments over the range of structures (Tables 1–4). Bond valence parameters taken from Brown, except those for Ag–Cl and Ag–Br which were taken from Hull and Berastegui (Appendix A).[25,26] With the exception of Rb_3RhCl_6, all of the compounds studied were found to be stable when exposed to ambient air for prolonged periods of time.

The rhodium-containing halide perovskites $(MA)_2AgRhX_6$ and $(MA)_2NaRhX_6$ were previously studied by Holzapfel et. al and will serve as a point of comparison throughout this manuscript.[16] Both compounds are site-ordered derivatives of the 2H hexagonal perovskite structure with $P\bar{3}m1$ space group symmetry. This structure contains infinite chains of face-sharing octahedra with the cation at the center of each octahedron alternating between Rh and Ag/Na (Figure 1a). Replacing methylammonium ion with the smaller cesium ion leads to the appearance

of a trigonal structure with $R\bar{3}m$ space group symmetry for both $Cs_2AgRhCl_6$ and $Cs_2NaRhCl_6$. This structure contains trimers of face-sharing octahedra bridged by corner-connected octahedra (Figure 1b). This structure is sometimes referred to as the 12R hexagonal perovskite structure and has previously been reported for Ba_2NiTeO_6 and $Cs_2AgCrCl_6$.[27,28] In Cs_2MRhCl_6 (M = Ag, Na) the rhodium cations occupy the middle octahedron in each trimer as well as the octahedral sites that share corners with neighboring trimers. Field dependent magnetization measurements taken at room temperature revealed a weakly negative susceptibility for $Cs_2AgRhCl_6$ (see Figure S14 in the Supporting Information), consistent with diamagnetism and the expected 3+ oxidation state for rhodium.

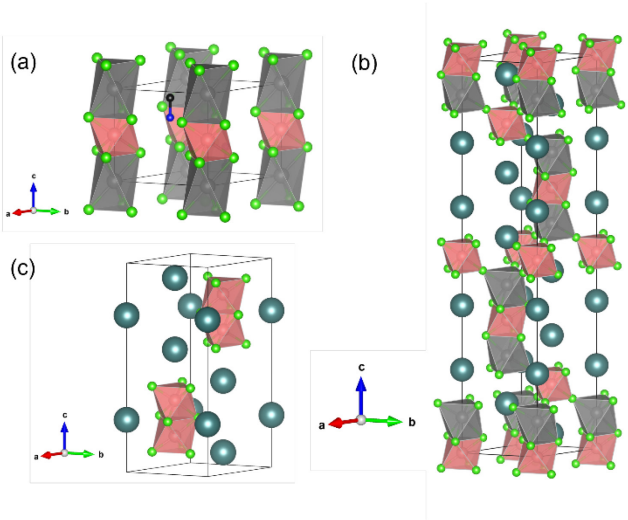

Figure 1: Crystal structure of (a) $(MA)_2AgRhCl_9$ (methylammonium ions not shown for clarity) (b) $Cs_2AgRhCl_6$ and (c) $Cs_3Rh_2Cl_9$. Ag- and Rh-centered octahedra shown in gray and pink, respectively. Blue-gray, green, blue, and black spheres represent Cs, Cl, N, and C, respectively.

Table 1: Summary of crystallographic information and BVS analysis for $Cs_2NaRhCl_6$ and $Cs_2AgRhCl_6$.

Composition	$Cs_2NaRhCl_6$	$Cs_2AgRhCl_6$
Space Group	$R\bar{3}m$	$R\bar{3}m$
a (Å)	7.26932(4)	7.23116(4)
c (Å)	36.3781(3)	36.3344(3)
Volume (Å^3)	1664.79(2)	1645.37(2)
Bond distances (Å)		
Cs(1)–Cl distances	3 × 3.772(4) 3 × 3.602(4) 6 × 3.640(2)	3 × 3.695(3) 3 × 3.638(3) 6 × 3.622(1)
Cs(2)–Cl distances	3 × 3.821(4) 3 × 3.769(4) 6 × 3.652(2)	3 × 3.797(3) 3 × 3.767(3) 6 × 3.628(1)
Rh(1)–Cl distances	6 × 2.354(3)	6 × 2.364(3)
Rh(2)–Cl distances	6 × 2.334(3)	6 × 2.363(2)
Ag/Na–Cl distances	3 × 2.690(5) 3 × 2.754(6)	3 × 2.649(3) 3 × 2.739(3)
Bond valences		
Cs(1)	1.15	1.20
Cs(2)	0.98	1.04
Rh(1)	3.02	2.78
Rh(2)	2.86	2.79
Ag/Na	1.09	1.16
Cl(1)	1.03	1.02
Cl(2)	1.02	1.04

$Rb_3Rh_2Br_9$, $Cs_3Rh_2Cl_9$, and $Cs_3Rh_2Br_9$ adopt a hexagonal structure with $P6_3/mmc$ space group symmetry. This structure can be described as a vacancy ordered variant of the 6H hexagonal perovskite structure.[29] It is adopted by several other $A_3M_2X_9$ phases, including $Cs_3Cr_2Cl_9$, $Cs_3Ru_2Cl_9$, and $Cs_3Mo_2Cl_9$. The structure consists of a repeating cubic–cubic–hexagonal $(cch)_2$ close packing of AX_3 layers (Figure 1c). The octahedral holes between the layers can be partially filled by smaller transition metal ions. In the $A_3Rh_2X_9$ phases studied here, the Rh^{3+} ions occupy the octahedral holes adjacent to the hexagonal-stacked layers leading to face-sharing $[Rh_2X_9]^{3-}$ dimers, while the octahedral holes that lie between cubic close packed layers are vacant, leaving the dimers isolated from one another.[30] The Rh^{3+} ions are displaced away from the shared face. This produces a structure where the bonds to the bridging halide ions in the shared face are 0.11−0.13 Å longer than those to the terminal halide ions that reside on periphery of the $[Rh_2X_9]^{3-}$ dimers. Similar displacements are seen for the Ag^+/Na^+ cations in the outer octahedra of the face-

sharing trimers in $Cs_2AgRhCl_6$ and $Cs_2NaRhCl_6$, but not for the Rh^{3+} ions in the central octahedron of the trimer.

In those $A_3M_2X_9$ compositions where the transition metal contains partially filled t_{2g} orbitals a metal-metal bond can form across the shared face. Consider for example, $Cs_3Ru_2Cl_9$ containing the $4d^5$ Ru^{3+} ion, and $Cs_3Mo_2Cl_9$ containing the $4d^3$ Mo^{3+} ion. In both compositions a metal-metal single bond is thought to form, leading to unexpectedly short metal-metal distances of 2.725 Å ($Cs_3Ru_2Cl_9$) and 2.648 Å ($Cs_3Mo_2Cl_9$).[31,32] By comparison the Rh–Rh distance is much longer in $Cs_3Rh_2Cl_9$, 3.050(4) Å, despite the fact that the metal-halide bonds are similar in length for all three compositions. The Rh–Rh distances are even longer in the bromides. This can be understood from the $4d^6$ configuration of Rh^{3+} which completely fills the t_{2g} orbital manifold and precludes formation of a metal-metal bond across the shared face.

Table 2: Summary of crystallographic information and BVS analysis for $A_3Rh_2X_9$.

Composition	$Cs_3Rh_2Cl_9$	$Cs_3Rh_2Br_9$	$Rb_3Rh_2Br_9$
Space Group	*P*6$_3$/*mmc*	*P*6$_3$/*mmc*	*P*6$_3$/*mmc*
a (Å)	7.1711(3)	7.4623(2)	7.2768(1)
c (Å)	17.7802(9)	18.6375(6)	18.5443(3)
Volume (Å^3)	791.83(8)	898.80(6)	850.40(3)
Bond distances (Å)			
Cs/Rb(1)–Cl/Br	6 × 3.589(2) 6 × 3.543(3)	6 × 3.735(1) 6 × 3.757(1)	6 × 3.687(3) 6 × 3.640(4)
Cs/Rb(2)–Cl/Br	6 × 3.596(1) 3 × 3.769(3) 3 × 3.629(3)	6 × 3.7411(8) 3 × 3.723(3) 3 × 3.959(3)	6 × 3.656(4) 3 × 3.991(4) 3 × 3.597(4)
Rh– Cl/Br	3 × 2.329(3) 3 × 2.450(3)	3 × 2.437(2) 3 × 2.561(2)	3 × 2.443(4) 3 × 2.551(4)
Rh–Rh	3.050(4)	3.214(5)	3.189(5)
Bond valences			
Cs/Rb(1)	1.48	1.40	1.10
Cs/Rb(2)	1.21	1.27	1.01
Rh	2.63	3.17	3.17
Cl/Br(1)	1.11	1.24	1.17
Cl/Br(2)	0.86	0.98	0.90

All four hybrid organic-inorganic compositions, A_4AgRhX_8 (A = BA, IPA; X = Cl, Br), were found to crystallize with monoclinic *C*2/*m* space group symmetry. The structure is derived from the *n* = 1 Ruddlesden-Popper (RP) parent structure which has *I*4/*mmm* space group symmetry. The symmetry is lowered to *C*2/*m* by the combined effects of long-range site-ordering of Ag^+ and Rh^{3+}

cations, as well as out-of-phase octahedral tilting along both the in-plane directions, referred to as (ϕϕ0)/(ϕϕ0) tilting in the Alexandrov nomenclature.[16] The crystal structures of $(BA)_4AgRhCl_8$ and $(IPA)_4AgRhCl_8$ are shown in Figure 2. While the Rh-centered octahedra are fairly regular, the Ag-centered octahedra show a significant axial compression, resulting in four longer bonds to the bridging (equatorial) halides and two shorter bonds to the terminal (axial) halides. This distortion is likely facilitated by the $4d^{10}$ configuration of the Ag^+ cation and has been observed in other layered halide double perovskites containing Ag^+ or Au^+.[33,34] The layered structure leads to significant issues with preferred orientation that can be partially but not completely alleviated using synchrotron PXRD in a capillary sample holder. This issue combined with the similar X-ray scattering lengths of Rh and Ag led to false minima in the Rietveld refinements that necessitated the use of bond distance constraints to get the best refinements, as discussed in the supporting information.

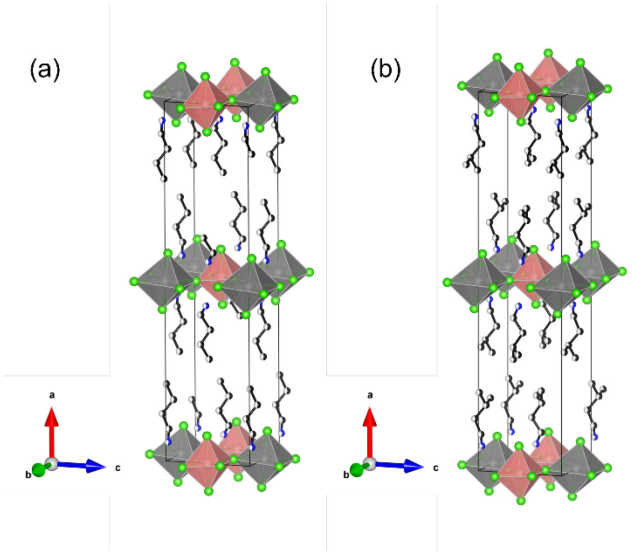

Figure 2: Crystal structures of (a) $(BA)_4AgRhCl_8$ and (b) $(IPA)_4AgRhCl_8$. The organic butylammonium and ispropylammonium cations are disordered over two positions, but only one-half of those cations are shown here for clarity. Ag- and Rh-centered octahedra shown in gray and pink, respectively. Green, blue, and black spheres represent Cs, Cl, N, and C, respectively. Hydrogen atoms are not shown.

Table 3: Summary of crystallographic information and BVS analysis for hybrid $n = 1$ Ruddlesden-Popper double perovskites.

Composition	$(BA)_4AgRhCl_8$	$(BA)_4AgRhBr_8$	$(IPA)_4AgRhCl_8$	$(IPA)_4AgRhBr_8$
Space Group	*C*2/*m*	*C*2/*m*	*C*2/*m*	*C*2/*m*
a (Å)	30.8912(1)	29.6644(2)	32.9985(3)	32.6743(2)
b (Å)	7.30859(1)	7.6661(5)	7.38254(6)	7.6852(3)
c (Å)	7.54631(1)	7.9453(5)	7.59283(7)	7.9409(4)
β (°)	90.293(3)	90.101(7)	90.007(2)	89.294(6)
Volume ($Å^3$)	1703.72(7)	1806.84(2)	1849.71(3)	1993.86(2)
Bond distances (Å)				
Rh–Cl/Br distances	4 × 2.384(5) 2 × 2.371(8)	4 × 2.510(4) 2 × 2.511(9)	4 × 2.384(4) 2 × 2.371(7)	4 × 2.510(4) 2 × 2.511(1)
Ag–Cl/Br distances	4 × 2.882(5) 2 × 2.434(8)	4 × 3.036(4) 2 × 2.607(1)	4 × 2.916(4) 2 × 2.434(7)	4 × 3.041(4) 2 × 2.608(7)
Bond valences				
Rh	2.67	3.06	2.67	3.06
Ag	1.25	1.07	1.20	1.06

The monoclinic structure of Rb_3RhCl_6 is isostructural to Cs_3ScCl_6 and Rb_3InCl_6.[35,36] One can envision this structure as a highly distorted variant of an ordered cubic double perovskite with stoichiometry $Rb_2RbRhCl_6$. The *C*2/*c* symmetry can be derived from the cubic double perovskite structure by rotating half of $[RhCl_6]^{3-}$ octahedra by ~45° about two of the three internal 4-fold axes of the octahedron. This breaks the corner connectivity of the cubic double perovskite structure, increasing the coordination number of the Rb^+ ions that were 6-coordinate and decreasing the coordination number of the Rb^+ ions that were 12-coordinate. The net effect is an arrangement of isolated $[RhCl_6]^{3-}$ polyatomic anions surrounded by charge compensating Rb^+ ions (Figure 3).

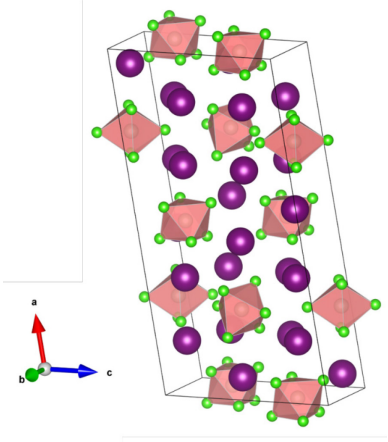

Figure 3: Crystal structure of Rb_3RhCl_6.

Table 4: Summary of BVS analysis for all Rb_3RhCl_6

Composition	Rb_3RhCl_6
Space Group	*C*2/*c*
a (Å)	24.9551(6)
b (Å)	7.56538(16)
c (Å)	12.2279(3)
α (°)	90
β (°)	100.0745(15)
γ (°)	90
Volume ($Å^3$)	2272.97(9)
Select Bond distances (Å)	
Rh(1)–Cl distances	2 × 2.36(1), 2 × 2.41(1), 2 × 2.35(1)
Rh(2)–Cl distances	2 × 2.37(1), 2 × 2.38(1), 2 × 2.26(2)
Bond valences	
Rb(1), Rb(2), Rb(3)	1.31, 0.95, 1.42
Rh(1), Rh(2)	2.72, 3.03
Cl(1), Cl(2), Cl(3)	1.26, 1.04, 1.04
Cl(4), Cl(5), Cl(6)	1.19, 0.98, 1.06

Diffuse Reflectance Spectroscopy (DRS)

DRS measurements were taken to probe the optical absorption characteristics of this family of compounds (Figure 4). To quantify the relative shifts in the energies of the optical transitions, the absorbance spectra were fitted to four gaussian peak profiles. The two peaks that are observed at longer wavelengths correspond to *d*-to-*d* transitions, while the higher energy peaks found in the UV are charge transfer excitations. Octahedral crystal field splitting energies (Δ_O) and Racah parameters (B) can be estimated from the energies of the *d*-to-*d* transitions using the Tanabe-Sugano diagram for a d^6 ion (see Table 5). An example of the peak fitting approach used, and estimates for the energies of the charge transfer excitations are given in the Supplemental Information (Figure S12, S13, Table S6).

We begin with the spectra of Rb_3RhCl_6, $(MA)_2NaRhCl_6$, and $Cs_2NaRhCl_6$ where the $[RhCl_6]^{3-}$ octahedra are clearly isolated from one another and a zero-dimensional electronic structure is expected. The two transitions that are found in the visible region can be attributed to the spin-allowed *d*-to-*d* transitions expected for an octahedrally coordinated metal ion with a low-spin d^6 octahedral configuration. The lower energy peak corresponds to the $^1A_{1g} \rightarrow {}^1T_{1g}$ transition and the higher energy peak to the $^1A_{1g} \rightarrow {}^1T_{2g}$ transition. These two peaks are in nearly identical positions,

~516 nm and 400-410 nm, respectively, for Rb_3RhCl_6 and $(MA)_2NaRhCl_6$. From the positions of these two peaks, one can estimate a crystal field splitting parameter $\Delta_o \approx 2.55$ eV and a Racah parameter, B ≈ 0.04 eV. The spectrum of $Cs_2NaRhCl_6$ is similar, but red-shifted by 10–20 nm, likely due to subtle differences in octahedral bond distances and angles. The absorbance peaks found in the UV can be assigned to ligand to metal charge transfer (LMCT) transitions. The lowest energy LMCT transition can be found near 320 nm for all three compositions.

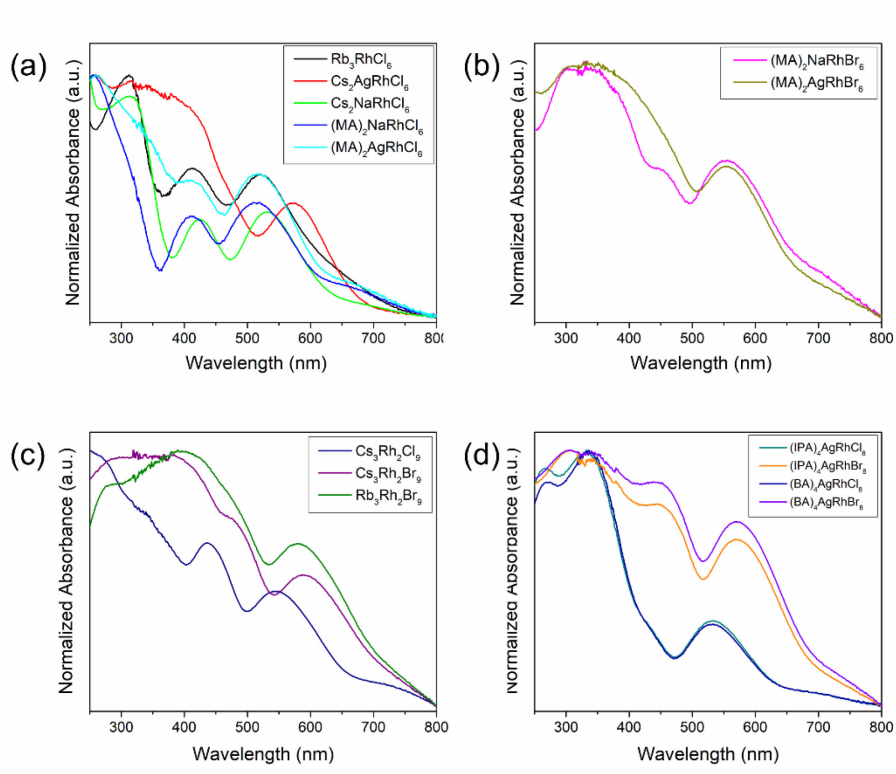

Figure 4: Absorption spectra for (a) chloride compositions, (b) $(MA)_2MRhBr_6$ compositions compositions, (c) $A_3Rh_2X_9$ compositions, and (d) hybrid *n* = 1 RP double perovskites.

The presence of Ag 5s and/or 4d valence orbitals near the Fermi energy raises the possibility of wider bands and higher dimensionality, provided the symmetry is conducive for Ag–Cl–Rh orbital mixing. The spectrum of $(MA)_2AgRhCl_6$ across the visible region is very similar to the compositions discussed above, suggesting its electronic structure is also zero-dimensional, as was concluded previously.[16] In contrast, the spectra of $Cs_2AgRhCl_6$ is significantly red-shifted with respect to the chloride compounds discussed thus far. For example, the $^1A_{1g} \rightarrow {}^1T_{1g}$ transition shifts to 575 nm in $Cs_2AgRhCl_6$. This suggests non-negligible Ag–Cl–Rh orbital mixing in the latter compound leading to an increase in the electronic dimensionality. This hypothesis will be further explored when the band structure calculations are discussed in the next section.

The cation-ordered 2H perovskites $(MA)_2NaRhBr_6$ and $(MA)_2AgRhBr_6$ are expected to possess zero-dimensional electronic structures, like their isostructural chloride analogs. The similar spectra of the two compounds (Figure 4b), indicates little mixing between Ag and Rh based orbitals, verifying this assumption. The *d*-to-*d* transitions are shifted to longer wavelengths (approximately 450 nm and 556 nm), reflecting a small decrease in $\Delta_o \approx 2.44$ eV and $B \approx 0.03$ eV. For both bromide and chloride compositions, the peaks in the absorption spectrum of the layered $n = 1$ RP phases (Figure 4d) are slightly red shifted (10-20 nm) from their 2H counterparts. This relatively subtle shift would seem to suggest that even though the crystal structure is unambiguously two dimensional, the electronic structure may not be as two dimensional as one might expect. The elongation of the Ag–Cl and Ag–Br bonds within the plane of the inorganic layers likely plays a role in this partial reduction of the electronic dimensionality. Changing the organic cation from IPA^+ to BA^+ has minimal effect on the spectra, which is not too surprising given the expectation that the organic cations do not make contributions to the electronic states near the Fermi energy.

Table 5: Peak maxima taken from Gaussian fitting profile center of gravity, octahedral crystal field splitting energies, and Racah parameters for all compositions.

Compounds	$^1A_{1g} \rightarrow {}^1T_{1g}$	$^1A_{1g} \rightarrow {}^1T_{2g}$	Δ_O (eV)	B (eV)
Rb_3RhCl_6	517 nm	409 nm	2.54	0.040
$Cs_2AgRhCl_6$	575 nm	483 nm	2.25	0.021
$Cs_2NaRhCl_6$	535 nm	422 nm	2.46	0.036
$(MA)_2NaRhCl_6$	516 nm	404 nm	2.55	0.044
$(MA)_2AgRhCl_6$	517 nm	417 nm	2.53	0.034
$(MA)_2NaRhBr_6$	556 nm	456 nm	2.34	0.028
$(MA)_2AgRhBr_6$	556 nm	450 nm	2.35	0.035
$Cs_3Rh_2Cl_9$	547 nm	444 nm	2.39	0.031
$Cs_3Rh_2Br_9$	595 nm	490 nm	2.19	0.024
$Rb_3Rh_2Br_9$	584 nm	478 nm	2.23	0.027
$(IPA)_4AgRhCl_8$	536 nm	435 nm	2.44	0.032
$(IPA)_4AgRhBr_8$	575 nm	464 nm	2.27	0.031
$(BA)_4AgRhCl_8$	536 nm	435 nm	2.43	0.031
$(BA)_4AgRhBr_8$	575 nm	462 nm	2.28	0.032

Finally, we consider the compounds that contain isolated $[Rh_2X_9]^{3-}$ face-sharing dimers. $Cs_3Rh_2Cl_9$ exhibits a spectrum similar to $Cs_2NaRhCl_6$ with a subtle red-shift of the *d*-to-*d* transitions and the addition of a feature at ~350 nm. The changes may be attributed to the breaking

of O_h symmetry due to the coulombic repulsion between the two rhodium cations, which lowers the point symmetry of each $[RhX_6]^{3-}$ octahedron to C_{3v} and the resulting dimer, $[Rh_2X_9]^{3-}$ to D_{3h}. As seen with the compounds discussed previously, the $A_3Rh_2Br_9$ (A = Cs, Rb) compositions are red-shifted with respect to $Cs_3Rh_2Cl_9$.

Electronic structure calculations

Electronic band structures were calculated to better understand how structural dimensionality and octahedral connectivity affect the electronic structure (Figure 5, S7–S11). Primitive unit cells were used in all cases to reduce the computational cost. For hybrid compositions the organic cation (MA^+ or IPA^+) was replaced with Cs^+ ions, to avoid complications arising from the dynamical disorder of the organic cations. This simplification is justified as it is generally accepted that neither Cs^+ nor protonated amines make significant contributions to the band structure near the Fermi level.[17,37] Hence, the electronic structure of $(IPA)_4AgRhX_8$ was approximated from calculations based on the hypothetical structure of Cs_4AgRhX_8 with the Ag, Rh, and halide positions fixed to the values obtained in the parent crystal structure. More information on the hypothetical structures used to approximate the $n = 1$ RP phases can be found in the supplemental information (Table S5).

In general, the band structures of all compositions possess similar features and are mainly differentiated by the dispersion of bands. Before describing the differences let us consider the common features, beginning with the band structure of $(MA)_2AgRhCl_6$ shown in Figure 5a. The highest occupied molecular orbitals (HOMO) of a $[RhCl_6]^{3-}$ polyatomic anion have Rh 4d (t_{2g}) – Cl 3p π^* character and the lowest unoccupied molecular orbitals (LUMO) have Rh 4d (e_g) – Cl 3p σ^* character. These two sets of frontier molecular orbitals are responsible for the three filled bands found between −1.1 and −0.7 eV (π^*) and the two empty bands found between +0.7 and +1.2 eV (σ^*), respectively. The bands immediately below the π^* valence bands (−1.3 to −1.8 eV) have significant silver character, as revealed by the partial density of states (PDOS) plots, and therefore can be assigned to have Ag 4d orbital parentage. The single band found above the σ^* conduction bands can be assigned as the Ag 5s band. The bands between −2 and −5.5 eV are predominantly Cl 3p in character, with those that are lower in energy having significant bonding overlap with the cations. The bands that have appreciable cesium character are located well above the Fermi energy, +4.5 eV and above. Notice that for the most part the bands are flat, consistent with the zero-

dimensional character assumed when discussing the optical spectra. The t_{2g} and e_g peak maxima in the PDOS are separated by roughly 2.0 eV, which is of the same magnitude as the Δ_0 (2.53 eV) value estimated from the DRS.

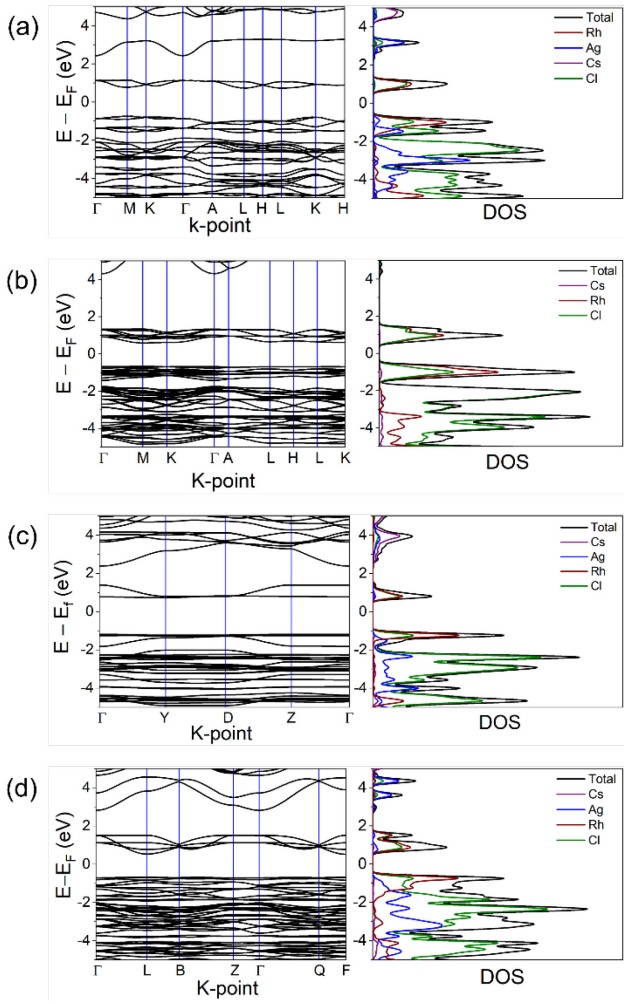

Figure 5: Band structure calculations for (a) $(MA)_2AgRhCl_6$, (b) $Cs_3Rh_2Cl_9$, (c) $(IPA)_4AgRhCl_8$, and (d) $Cs_2AgRhCl_6$.

The band structure of $Cs_3Rh_2Cl_9$ is shown in Figure 5b. Because there are now four Rh atoms per unit cell, the number of Rh 4d bands increases by a factor of four. Interactions across the shared face lead to a wider energy spread of the π^* and σ^* bands, but the individual bands are still rather flat, which is not surprising given the minimal orbital overlap between the neighboring $[Rh_2Cl_9]^{3-}$ dimers. The relatively small differences between the electronic structure of a $[Rh_2Cl_9]^{3-}$ dimer and a $[RhCl_6]^{3-}$ octahedron are likely responsible for the small red-shift seen in the optical absorption

peaks of $Cs_3Rh_2Cl_9$ when compared to Rb_3RhCl_6 and $(MA)_2MRhCl_6$ (M = Na, Ag). The bromide compositions exhibit increased band dispersion compared to chlorides.

The band structure of $(IPA)_4AgRhCl_8$ possesses slightly broader σ^* conduction bands (Figure 5c). The dispersion for one of the bands is ~0.6 eV along the Γ to Y and D to Z directions. These directions are parallel to the inorganic layers and represent a shift toward a 2D electronic structure. This can be attributed to hybridization between orbitals with Rh $4d_{x^2-y^2}$ –Cl 3s/3p σ^* character and the Ag 5s orbitals. The width of this band would undoubtedly be larger were it not for the elongation of the Ag–Cl bonds within the inorganic layer. In contrast, the bands are almost perfectly flat along the Γ to Z direction. This is expected given the negligible electronic coupling through the organic cations that separate inorganic layers. We can also use the band structure calculations to help with assignments of the charge transfer transitions. The difference in energies between sets of orbitals can be approximated by the difference in the energies of the peaks from the DOS plots. The lowest energy LMCT has an energy difference of approximately 3.5 eV. This is in agreement with the initial onset of the CT absorption seen in the DRS measurements (3.5 eV). Assigning specific transitions beyond the initial onset is not trivial. The mix of low-lying Cl 3p and Ag 4d bands (−2 eV to −5 eV) likely contribute to various LMCT and MMCT transitions. Moreover, the flat valence bands make it so the energies of the direct and indirect transitions are almost identical. This phenomenon has been observed in other computational studies of layered perovskites.[38]

The band structure for $Cs_2AgRhCl_6$ with the 12R structure is shown in Figure 5d. The most important thing to note is that it has more disperse Rh 4d–Cl 3s/3p σ^* bands (~1.0 eV) than any of the compounds discussed thus far. The four σ^* bands can be broken down into two groups. The two broader bands can be assigned to the Rh octahedra in the corner connected position, as this geometry allows for mixing of the Ag and Rh states. These bands are wider than found in $(IPA)_4AgRhCl_8$ because the Ag-centered octahedra are much less distorted in $Cs_2AgRhCl_6$. There are also two narrower bands associated with the Rh octahedron in the middle of the trimers, which is electronically isolated as it was in the 2H structure of $(MA)_2AgRhCl_6$. The increased band dispersion lowers the excitation energy of the *d*-to-*d* and LMCT transitions, which leads to the significant red shift seen in the optical spectrum. While these features are consistent with an increase in dimensionality, the lack of dispersion for the σ^* bands in the Z to Γ direction suggests that $Cs_2AgRhCl_6$ is best described as possessing a 2D electronic structure. A finding that is not

entirely obvious from the crystal structure and can be attributed to the lack of hybridization between Rh 4*d*–Cl 3s/3p σ^* and Ag 5s orbitals through the face-sharing connection.

For the sake of completeness, the hypothetical band structure of cubic $Cs_2AgRhCl_6$ (a = 10.084 Å) was also calculated and is shown in Figure S11. It possesses Rh 4d–Cl 3s/3p σ^* bands that are roughly 2 eV wide and a direct band gap. However, the valence bands with Rh 4d–Cl 3s/3p π^* character are still quite narrow, with widths on the order of 0.3 eV. This result agrees with the earlier calculations of Varadwaj and Marquez.[15]

DISCUSSION

The initial goal of this research was to synthesize the cubic double perovskite $Cs_2AgRhCl_6$ and assess the suitability of its electronic structure for photovoltaic applications. While this compound was successfully prepared, it crystallizes with the 12R hexagonal perovskite structure instead of the cubic double perovskite structure. The two structures share several common features. Both exhibit an ordered arrangement of Ag^+ and Rh^{3+}. Both can be described as having a close-packed arrangement of cesium and chloride ions, with the smaller Ag^+ and Rh^{3+} cations filling octahedral holes. Where they differ from one another is in the packing of the cesium chloride layers and the connectivity of the octahedra.

Empirical predictions regarding the stability of cubic structure with respect to various hexagonal perovskite structures (2H, 6H, 9R, 12R, etc.) are typically based on the tolerance factor, which relies on ionic radii (r_A, r_B, r_X) to estimate how well the A-site cations fill the cavities of the network of corner-connected octahedra.[39] The concept of tolerance factor can be extended to double perovskites by averaging the ionic radii of the two B-site metals (r_{B1}, r_{B2}), yielding the following equation:

$$t = (r_A + r_X)/[\sqrt{2}(\left(\frac{r_{B1}+r_{B2}}{2}\right) + r_X)]$$

A tolerance factor of unity, t = 1, indicates a perfect fit for the A-site cation in the cubic perovskite structure. In oxide and fluoride perovskites, a smaller tolerance factor (t < 1) is typically associated with octahedral tilting distortions, while a tolerance factor greater than unity (t > 1) indicates that the cuboctahedral void is not large enough to accommodate the A-site cation. When this occurs, hexagonal perovskite polytypes (12R, 9R, 6H, 2H, …) are often found to be more stable than the cubic structure.

Table 6: The M–Cl distances, tolerance factors, and crystal structures of several $Cs_2AgM^{3+}Cl_6$ compositions.

Compound	M^{3+} ionic radius (Å)	M^{3+}–Cl dist. (Å)	Tolerance factor	Structure type	Reference
$Cs_2AgBiCl_6$	1.03	2.681	0.900	cubic DP	[13]
$Cs_2AgTlCl_6$	0.885	2.574	0.923	cubic DP	[40]
$Cs_2AgInCl_6$	0.80	2.512	0.937	cubic DP	[41]
$Cs_2AgSbCl_6$	0.76	2.628	0.944	cubic DP	[42]
$Cs_2AgRhCl_6$	0.665	2.364	0.960	12R	this work
$Cs_2AgFeCl_6$	0.645	2.382	0.964	cubic DP	[43]
$Cs_2AgCrCl_6$	0.615	2.357	0.969	12R	[27]

The tolerance factor values of known Cs_2AgMCl_6 compositions were calculated and are given in Table 6. The ionic radii values tabulated by Shannon were used for the calculations.[44] There are several caveats to using the tolerance factor for compositions containing the heavier halide ions. Firstly, ionic radii are less reliable at predicting the bond distances in compounds containing polarizable anions like Cl^- and Br^-. For example, the In–Cl distance predicted by ionic radii, $r_{In} + r_{Cl}$ = 0.80 Å + 1.81 Å = 2.61 Å, is considerably longer than the experimental distance of 2.512 Å seen in $Cs_2AgInCl_6$. The imprecision of ionic radii can also be seen by comparing the relative trends in ionic radii and experimental M^{3+}–Cl bond distances in the second and third columns of Table 3. Secondly, even when the tolerance factor is considerably below $t = 1$ octahedral tilting is not usually seen in the heavier halide perovskites.[45] Keeping these considerations in mind, we see that the two compositions that adopt the 12R structure have the shortest M^{3+}–Cl bond distances. If the ionic radii were more reliable for these compounds, $Cs_2AgRhCl_6$ and $Cs_2AgCrCl_6$ would have larger tolerance factors than $Cs_2AgFeCl_6$. Thus, the expected trend for the cubic structure to give way to the 12R structure as the tolerance factor increases is realized.

The trends highlighted in Table 3 suggest that $Cs_2AgRhCl_6$ lies near the boundary separating the 12R and cubic double perovskite structure types, implying that the two structures have very similar energies. This conclusion is supported by the total energies obtained for each structure from the DFT calculations, −2335.94 Ry per formula unit for the 12R structure, and −2335.92 Ry for the cubic double perovskite structure. The two values are essentially the same within the uncertainties associated with the calculations. Reducing the tolerance factor via chemical substitutions may alter the energy landscape sufficiently to stabilize a cubic double perovskite

structure with Rh^{3+} and Ag^{+} on the octahedral sites. The most logical choice would be to replace Cs^{+} with the smaller Rb^{+} ion, but synthetic attempts to prepare $Rb_2AgRhCl_6$ and related compositions did not lead to formation of a single phase product. High pressures can sometimes be used to make metastable cubic perovskites, so it would stand to reason that high pressure synthesis may be another approach to stabilize the cubic structure.

Even though the goal of preparing a cubic double perovskite was not realized, the variety of structures explored here offer considerable insight into the electronic structures of ternary and quaternary rhodium halides. The calculated widths of the Rh e_g (σ^*) bands for various compounds are summarized in Table 7. We hypothesize that the σ^* band width can be used as a proxy for the dimensionality of the electronic structure. When the Rh-centered octahedra are isolated from one another and surrounded by electropositive alkali metal cations, as is the case for $(MA)_2NaRhCl_6$ and $Cs_2NaRhCl_6$, a zero-dimensional electronic structure is expected, and the Rh 4d–Cl 3s/3p σ^* bandwidth is on the order of 0.4 to 0.5 eV.

Table 7: The calculated width of the Rh e_g σ^* bands, and the wavelength of the lowest energy t_{2g} to e_g electronic transition ($^1A_{1g} \rightarrow {}^1T_{1g}$) for several ternary and quaternary compositions containing $[RhCl_6]^{3-}$ octahedra.

Composition	σ^* band width (eV)	$^1A_{1g} \rightarrow {}^1T_{1g}$ transition
$(MA)_2NaRhCl_6$	0.42 eV	516 nm
$(MA)_2AgRhCl_6$	0.42 eV	517 nm
$Cs_2NaRhCl_6$	0.52 eV	535 nm
$(IPA)_4AgRhCl_8$	0.66 eV	536 nm
$(Ba)_4AgRhCl_8$	0.66 eV	536 nm
$Cs_3Rh_2Cl_9$	0.69 eV	547 nm
$Cs_2AgRhCl_6$ (12R)	0.99 eV	579 nm
$Cs_2AgRhCl_6$ (Cubic DP)*	2.02 eV	-

*Denotes hypothetical structure

When Ag^{+} cations are introduced, there is a possibility for an increase in dimensionality due to hybridization between orbitals with Rh 4d–Cl 3s/3p σ^* character and the Ag 5s orbitals. The extent of this hybridization depends on the manner in which the polyhedra are connected. When the Rh- and Ag-centered octahedra share faces, the highly bent Rh–Cl(Br)–Rh bonds are not favorable for orbital overlap and hybridization. Hence, the electronic structure of $(MA)_2AgRhCl_6$

is very similar to $(MA)_2NaRhCl_6$. However, when the octahedra share corners, hybridization that increases the electronic dimensionality does occur. The layered Ruddlesden-Popper phases have the desired corner-connected topology in the *xy*-plane, but the orbital overlap is diminished by the elongation of the Ag bonds to the bridging halide ions. This limits the orbital overlap between Ag 5s orbitals and the Rh–Cl/Br σ^* orbitals, and the width of the bands that arise from these orbitals increases only modestly from the zero-dimensional compounds.

A further increase in dimensionality is realized in $Cs_2AgRhCl_6$, which adopts the 12R structure. The structure exhibits nearly linear Ag–X–Rh bonds (175.9°) through the corner connected octahedra, and the Ag–Cl bonds are much shorter (2.649 Å) than seen in the layered Ruddlesden-Popper phases. This geometry results in a pseudo two-dimensional electronic structure with σ^* bands that are more than twice the width seen in the zero-dimensional compounds. The poor orbital overlap through the central Rh^{3+} ion of the face-sharing $[Ag_2RhCl_{12}]^{7-}$ trimers prevents realization of a fully three-dimensional band structure. The band structure calculations suggest that if the cubic double perovskite structure could be stabilized the σ^* bandwidth would double yet again.

$Cs_2AgRhCl_6$ may have some potential as a photovoltaic absorber. Attractive features include a direct band gap that lies close to the Shockley-Queisser limit (~1.8 eV absorption onset). Furthermore, the increased conduction band width should impart respectable electron mobility. Limiting features include anisotropic carrier transport resulting from the 2D nature of the electronic structure, and the lack of dispersion seen in the Rh–Cl π^* bands, which will likely result in low hole mobility. Finding a way to stabilize the cubic double perovskite structure, such as with high pressure synthesis, would eliminate the former concern, but the not the latter. Even if the presence of narrow valence bands is not problematic, the scarcity and high cost of rhodium is a significant obstacle to any potential applications.

CONCLUSIONS

In summary, ten new ternary and quaternary halide compositions containing rhodium were synthesized and investigated by the means of diffuse reflectance spectroscopy (DRS) and electronic band structure calculations. Analysis of the DRS data reveals the presence of both *d*-to-*d* and charge transfer transitions. Electronic band structure calculations show that the inclusion of

Ag^+ ions can lead to a higher dimensional electronic structure provided the Ag- and Rh-centered octahedra share corners and not faces. One of the compounds studied here, $Cs_2AgRhCl_6$, has a pseudo-2D electronic structure that exhibits a pronounced broadening of the σ^* conduction bands and a considerably smaller band gap than the other chloride compositions studied here. These features can be attributed to its crystal structure which contains two-dimensional slabs of corner connected Ag- and Rh-centered octahedra.

ASSOCIATED INFORMATION

Supporting Information

The supporting information is available free of charge at (LINK)

Details of RP-phase refinement methodology; Rietveld refinement of SPXRD patterns at 295K (Figures S1, S2); Crystallographic information of all compositions (Tables S1, S2); Comparison of Pawley fitting of the SPXRD data with the *I*4/*mmm*, *Cmca*, and *Cmmm* models for $(BA)_4AgRhCl_8$ (Figure S3); Comparison of Pawley fitting of the SPXRD data with the *I*4/*mmm*, *Cmca*, and *Cmmm* models for $(IPA)_4AgRhCl_8$ (Figure S4); Comparison of Pawley fitting of the SPXRD data with the *I*4/*mmm*, *Cmca*, and *Cmmm* models for $(BA)_4AgRhBr_8$ (Figure S5); Comparison of Pawley fitting of the SPXRD data with the *I*4/*mmm*, *Cmca*, and *Cmmm* models for $(IPA)_4AgRhBr_8$ (Figure S6); Comparison of the R_{wp} values found for Rietveld refinements of SPXRD data with the *C*2/*m* and *Cmmm* models (Table S3); Rigid body parameters for the organic moieties (Table S4); Structure details for the hypothetical primitive cells of $Cs_4AgRhCl_8$ and $Cs_4AgRhBr_8$ used for DFT calculations (Table S5); Results of electronic band structure calculations (Figures S7, S8, S9, S10, S11); Gaussian fits on the diffused reflectance spectroscopy (DRS) data (Figure S12, S13); Peak fitting data from DRS analysis of all compounds. The direct/indirect nature of band gap determined from electronic band structure (Table S7); Isothermal magnetization of $Cs_2AgRhCl_6$ at room temperature (Figure S14).

AUTHOR INFORMATION

Supporting Information

The Supporting Information is available free of charge on the ACS Publications website.

Details of diffraction experiments, crystallographic data (PDF)

ORCID

David Liu: 0000-0001-5136-3037

Noah P. Holzapfel: 0000-0002-4566-4033

Alexander Milder: 0000-0002-3143-1482

Patrick M. Woodward: 0000-0002-3441-2148

Author Contributions

The manuscript was written through contributions of all authors. Equal contribution of authorship is denoted with $^{\varepsilon}$. All authors have given approval to the final version of the manuscript.

Notes

The authors declare no competing financial interest.

ACKNOWLEDGEMENT

This work is dedicated to Professor C. N. R. Rao on the occasion of his 90th birthday. His numerous contributions to the fields of solid state chemistry and materials chemistry serve as an inspiration to multiple generations of scientists. Funding was provided by the National Science Foundation under award number DMR-2003793 and the National Science Foundation NRT Program under the award number 1922666. Special thanks to the 11 BM beamline staff for collection of synchrotron X-ray diffraction measurements. Use of the Advanced Photon Source at Argonne National Laboratory was supported by the U.S. Department of Energy, Office of Science, Office of Basic Energy Sciences, under Contract No. DE-AC02-06CH11357.

REFERENCES:

(1) Kojima, A.; Teshima, K.; Shirai, Y.; Miyasaka, T. Organometal Halide Perovskites as Visible-Light Sensitizers for Photovoltaic Cells. *J. Am. Chem. Soc.* **2009**, 131, 17, 6050–6051. https://doi.org/10.1021/ja809598r

(2) Adhyaksa, G. W. P.; Veldhuizen, L. W.; Kuang, Y.; Brittman, S.; Schropp, R. E. I.; Garnett, E. C. Carrier Diffusion Lengths in Hybrid Perovskites: Processing, Composition, Aging, and Surface Passivation Effects. *Chem. Mater.* **2016**, *28*, 5259–5263. https://doi.org/10.1021/acs.chemmater.6b00466.

(3) Grätzel, M. The Rise of Highly Efficient and Stable Perovskite Solar Cells. *Acc. Chem. Res.* **2017**, *50*, 487–491. https://doi.org/10.1021/acs.accounts.6b00492.

(4) Correa-Baena, J.-P.; Saliba, M.; Buonassisi, T.; Grätzel, M.; Abate, A.; Tress, W.; Hagfeldt, A. Promises and Challenges of Perovskite Solar Cells. *Science* **2017**, *358*, 739–744. https://doi.org/10.1126/science.aam6323.

(5) Wang, K.; Liu, C.; Du, P.; Zheng, J.; Gong, X. Bulk Heterojunction Perovskite Hybrid Solar Cells with Large Fill Factor. *Energy Environ. Sci.* **2015**, *8*, 1245–1255. https://doi.org/10.1039/C5EE00222B.

(6) Yang, W. S.; Noh, J. H.; Jeon, N. J.; Kim, Y. C.; Ryu, S.; Seo, J.; Seok, S. Il. High-Performance Photovoltaic Perovskite Layers Fabricated through Intramolecular Exchange. *Science* **2015**, *348*, 1234–1237. https://doi.org/10.1126/science.aaa9272.

(7) Bi, D.; Tress, W.; Dar, M. I.; Gao, P.; Luo, J.; Renevier, C.; Schenk, K.; Abate, A.; Giordano, F.; Correa Baena, J.-P.; Decoppet, J.-D.; Zakeeruddin, S. M.; Nazeeruddin, M. K.; Grätzel, M.; Hagfeldt, A. Efficient Luminescent Solar Cells Based on Tailored Mixed-Cation Perovskites. *Sci. Adv.* **2016**, *2*, :e150117. https://doi.org/10.1126/sciadv.1501170.

(8) NREL, *Best Research-Cell Efficiency Chart*; https://www.nrel.gov/pv/cell-efficiency.html (accessed 2023-04-22).

(9) Zhang, S.; Han, G. Intrinsic and Environmental Stability Issues of Perovskite Photovoltaics. *Progress in Energy* **2020**, *2*. 022002. https://doi.org/10.1088/2516-1083/ab70d9.

(10) Boyd, C. C.; Cheacharoen, R.; Leijtens, T.; McGehee, M. D. Understanding Degradation Mechanisms and Improving Stability of Perovskite Photovoltaics. *Chem. Rev.* **2019**, *119*, 3418–3451. https://doi.org/10.1021/acs.chemrev.8b00336.

(11) Kangsabanik, J.; Sugathan, V.; Yadav, A.; Yella, A.; Alam, A. Double Perovskites Overtaking the Single Perovskites: A Set of New Solar Harvesting Materials with Much Higher Stability and Efficiency. *Phys. Rev. Mater.* **2018**, *2*, 055401. https://doi.org/10.1103/PhysRevMaterials.2.055401.

(12) Wei, F.; Deng, Z.; Sun, S.; Zhang, F.; Evans, D. M.; Kieslich, G.; Tominaka, S.; Carpenter, M. A.; Zhang, J.; Bristowe, P. D.; Cheetham, A. K. Synthesis and Properties of a Lead-Free Hybrid Double Perovskite: $(CH_3NH_3)_2AgBiBr_6$. *Chem. Mater.* **2017**, *29*, 1089–1094. https://doi.org/10.1021/acs.chemmater.6b03944.

(13) McClure, E. T.; Ball, M. R.; Windl, W.; Woodward, P. M. Cs_2AgBiX_6 (X = Br, Cl): New Visible Light Absorbing, Lead-Free Halide Perovskite Semiconductors. *Chem. Mater.* **2016**, *28*, 1348–1354. https://doi.org/10.1021/acs.chemmater.5b04231.

(14) Meng, W.; Wang, X.; Xiao, Z.; Wang, J.; Mitzi, D. B.; Yan, Y. Parity-Forbidden Transitions and Their Impact on the Optical Absorption Properties of Lead-Free Metal Halide Perovskites and Double Perovskites. *J. Phys. Chem. Lett.* **2017**, *8*, 2999–3007. https://doi.org/10.1021/acs.jpclett.7b01042.

(15) Varadwaj, P. R.; Marques, H. M. The $Cs_2AgRhCl_6$ Halide Double Perovskite: A Dynamically Stable Lead-Free Transition-Metal Driven Semiconducting Material for Optoelectronics. *Front. Chem.* **2020**, *8*. https://doi.org/10.3389/fchem.2020.00796.

(16) Holzapfel, N. P.; Milder, A.; Woodward, P. M. Hybrid Organic–Inorganic Halide Derivatives of the 2H Hexagonal Perovskite Structure. *Chem. Mater.* **2022**, *34*, 7705–7711. https://doi.org/10.1021/acs.chemmater.2c00688.

(17) McClure, E. T.; McCormick, A. P.; Woodward, P. M. Four Lead-Free Layered Double Perovskites with the $n = 1$ Ruddlesden–Popper Structure. *Inorg. Chem.* **2020**, *59*, 6010–6017. https://doi.org/10.1021/acs.inorgchem.0c00009.

(18) Cohelo, A. TOPAS-Academic. *Powder Diffr.* **2007**, 312–317

(19) Momma, K.; Izumi, F. *VESTA 3* for Three-Dimensional Visualization of Crystal, Volumetric and Morphology Data. *J. Appl. Crystallogr.* **2011**, *44*, 1272–1276. https://doi.org/10.1107/S0021889811038970.

(20) Giannozzi, P.; Baroni, S.; Bonini, N.; Calandra, M.; Car, R.; Cavazzoni, C.; Ceresoli, D.; Chiarotti, G. L.; Cococcioni, M.; Dabo, I. QUANTUM ESPRESSO: A Modular and Open-Source Software Project for Quantum Simulations of Materials. *J. Phys.: Cond. Matter* **2009**, *21*, 395502. https://doi.org/10.1088/0953-8984/21/39/395502

(21) Giannozzi, P.; Andreussi, O.; Brumme, T.; Bunau, O.; Nardelli, M. B.; Calandra, M.; Car, R.; Cavazzoni, C.; Ceresoli, D.; Cococcioni, M. Advanced Capabilities for Materials Modelling with Quantum ESPRESSO. *J. Phys.: Cond. Matter* **2017**, *29*, 465901. https://doi.org/10.1088/1361-648X/aa8f79

(22) Satomichi Nishihara. S. BURAI 1.3 A GUI of Quantum ESPRESSO; https://nisihara.wixsite.com/burai (accessed 2020-11-11).

(23) Perdew, J. P.; Burke, K.; Ernzerhof, M. Generalized Gradient Approximation Made Simple. *Phys. Rev. Lett.* **1996**, *77*, 3865–3868. https://doi.org/10.1103/PhysRevLett.77.3865.

(24) Pack, J. D.; Monkhorst, H. J. Special Points for Brillouin-Zone Integrations—A Reply. *Phys Rev B* **1977**, *16*, 1748. https://doi.org/10.1103/PhysRevB.13.5188

(25) Hull, S.; Berastegui, P. Crystal Structures and Ionic Conductivities of Ternary Derivatives of the Silver and Copper Monohalides—II: Ordered Phases within the $(AgX)_x$–$(MX)_{1-x}$ and $(CuX)_x$–$(MX)_{1-x}$ (M= K, Rb and Cs; X= Cl, Br and I) Systems. *J. Solid State Chem.* **2004**, *177*, 3156–3173. https://doi.org/10.1016/j.jssc.2004.05.004

(26) Brown, I. D. *The Chemical Bond in Inorganic Chemistry: The Bond Valence Model*; Oxford university press, 2016; Vol. 27.

(27) Zhou, Y.; Askar, A. M.; Pöhls, J.; Iyer, A. K.; Oliynyk, A. O.; Shankar, K.; Mar, A. Hexagonal Double Perovskite $Cs_2AgCrCl_6$. *Z. Anorg. Allg. Chem.* **2019**, *645*, 323–328. https://doi.org/10.1002/zaac.201800351.

(28) Koehl, P.; Mueller, U.; Reinen, D. Ba_2NiTeO_6 - Eine Neue Verbindung in Der Reihe Der Hexagonalen Perowskite. *Z. Anorg. Allgemeine Chem.* **1972**, *392*, 124–136. https://doi.org/10.1002/zaac.19723920204.

(29) Wessel, G. J.; IJdo, D. J. W. The Crystal Structure of $Cs_3Cr_2Cl_9$. *Acta Crystallogr.* **1957**, *10*, 466–468. https://doi.org/10.1107/S0365110X57001577.

(30) Nguyen, L. T.; Cava, R. J. Hexagonal Perovskites as Quantum Materials. *Chem. Rev.* **2021**, *121*, 2935–2965. https://doi.org/10.1021/acs.chemrev.0c00622.

(31) Darriet, J. Crystal Structure and Magnetic Properties of the (Ru2Cl9)3- Ion in $Cs_3Ru_2Cl_9$. *Revue de Chimie Minerale* **1981**, *18*, 27–32.

(32) Stranger, R.; Grey, I. E.; Madsen, I. C.; Smith, P. W. Structure Systematics in $A_3Mo_2X_9$, X = Cl, Br, I, from Rietveld Refinement of X-Ray Powder Data. *J. Solid State Chem.* **1987**, *69*, 162–170. https://doi.org/10.1016/0022-4596(87)90022-3.

(33) Elliott, N.; Pauling, L. The Crystal Structure of Cesium Aurous Auric Chloride, $Cs_2AuAuCl_6$ and Cesium Argentous Auric Chloride, $Cs_2AgAuCl_6$. *J. Am. Chem. Soc.* **1938**, *60*, 1846–1851. https://doi.org/10.1021/ja01275a037.

(34) Connor, B. A.; Leppert, L.; Smith, M. D.; Neaton, J. B.; Karunadasa, H. I. Layered Halide Double Perovskites: Dimensional Reduction of $Cs_2AgBiBr_6$. *J Am Chem Soc* **2018**, *140*, 5235–5240. https://doi.org/10.1021/jacs.8b01543.

(35) Ward, M. D.; Ibers, J. A. Cs_3ScCl_6. *Acta Crystallogr Sect E Struct Rep Online* **2014**, *70* (6), i25–i25. https://doi.org/10.1107/S1600536814009799.

(36) Majher, J. D.; Gray, M. B.; Liu, T.; Holzapfel, N. P.; Woodward, P. M. Rb_3InCl_6 : A Monoclinic Double Perovskite Derivative with Bright Sb^{3+}-Activated Photoluminescence. *Inorg. Chem.* **2020**, *59*, 14478–14485. https://doi.org/10.1021/acs.inorgchem.0c02248.

(37) Giorgi, G.; Fujisawa, J.-I.; Segawa, H.; Yamashita, K. Small Photocarrier Effective Masses Featuring Ambipolar Transport in Methylammonium Lead Iodide Perovskite: A Density Functional Analysis. *J. Phys. Chem. Lett.* **2013**, *4*, 4213–4216. https://doi.org/10.1021/jz4023865.

(38) Mao, L.; Teicher, S. M. L.; Stoumpos, C. C.; Kennard, R. M.; DeCrescent, R. A.; Wu, G.; Schuller, J. A.; Chabinyc, M. L.; Cheetham, A. K.; Seshadri, R. Chemical and Structural Diversity of Hybrid Layered Double Perovskite Halides. *J. Am. Chem. Soc.* **2019**, *141*, 19099–19109. https://doi.org/10.1021/jacs.9b09945.

(39) Goldschmidt, V. M. Die Gesetze Der Krystallochemie. *Naturwissenschaften* **1926**, *14*, 477–485. https://doi.org/10.1007/BF01507527.

(40) Slavney, A. H.; Leppert, L.; Saldivar Valdes, A.; Bartesaghi, D.; Savenije, T. J.; Neaton, J. B.; Karunadasa, H. I. Small-Band-Gap Halide Double Perovskites. *Angew. Chem. Int. Ed.* **2018**, *57*, 12765–12770. https://doi.org/10.1002/anie.201807421.

(41) Gray, M. B.; Majher, J. D.; Strom, T. A.; Woodward, P. M. Broadband White Emission in $Cs_2AgIn_{1-x}Bi_xCl_6$ Phosphors. *Inorg. Chem.* **2019**, *58*, 13403–13410. https://doi.org/10.1021/acs.inorgchem.9b02299.

(42) Zhou, J.; Rong, X.; Molokeev, M. S.; Zhang, X.; Xia, Z. Exploring the Transposition Effects on the Electronic and Optical Properties of $Cs_2AgSbCl_6$ *via* a Combined Computational-Experimental Approach. *J. Mater. Chem. A* **2018**, *6*, 2346–2352. https://doi.org/10.1039/C7TA10062K.

(43) Yin, H.; Xian, Y.; Zhang, Y.; Chen, W.; Wen, X.; Rahman, N. U.; Long, Y.; Jia, B.; Fan, J.; Li, W. An Emerging Lead-Free Double-Perovskite $Cs_2AgFeCl_6$:In Single Crystal. *Adv. Funct. Mater.* **2020**, *30*. https://doi.org/10.1002/adfm.202002225.

(44) Shannon, R. D. Revised Effective Ionic Radii and Systematic Studies of Interatomic Distances in Halides and Chalcogenides. *Acta Crystallographica Section A* **1976**, *32*, 751–767. https://doi.org/10.1107/S0567739476001551.

(45) Linaburg, M. R.; McClure, E. T.; Majher, J. D.; Woodward, P. M. $Cs_{1-x}Rb_xPbCl_3$ and $Cs_{1-x}Rb_xPbBr_3$ Solid Solutions: Understanding Octahedral Tilting in Lead Halide Perovskites. *Chem. Mater.* **2017**, *29*, 3507–3514. https://doi.org/10.1021/acs.chemmater.6b05372.

TOC Graphic